Journal of Alloys and Compounds 509 (2011) 1069–1078

Contents lists available at ScienceDirect

Journal of Alloys and Compounds

journal homepage: www.elsevier.com/locate/jallcom

Effect of Ce on microstructure, mechanical properties and corrosion behavior of high-pressure die-cast Mg–4Al-based alloy

Jinghuai Zhang[a], Zhe Leng[a], Milin Zhang[a,*], Jian Meng[b,*], Ruizhi Wu[a]

[a] Key Laboratory of Superlight Materials & Surface Technology, Ministry of Education, Harbin Engineering University, No. 145 Nantong Street, Nangang District, Harbin, Heilongjiang 150001, China
[b] State Key Laboratory of Rare Earth Resources Utilization, Changchun Institute of Applied Chemistry, Chinese Academy of Sciences, Changchun 130022, China

ARTICLE INFO

Article history:
Received 18 May 2010
Received in revised form
25 September 2010
Accepted 28 September 2010
Available online 8 October 2010

Keywords:
Mg–Al–Ce–Mn alloy
Microstructure
Mechanical properties
Corrosion

ABSTRACT

Mg–4Al–*x*Ce–0.3Mn (*x* = 0, 1, 2, 4 and 6 wt.%) alloys were prepared by high-pressure die-casting. The microstructures, mechanical properties and corrosion behavior were investigated. The cross-section of test bar is divided into the fine skin region and the relatively coarse interior region by a narrow band. The dendritic arm spacing is greatly reduced and the secondary phases $Al_{11}Ce_3$ and $(Al, Mg)_2Ce$ with the former being the dominant one substitute the $Mg_{17}Al_{12}$ phase with addition of Ce. When Ce content reaches 4 wt.%, the alloy exhibits an optimal cost performance ratio. The improved mechanical properties maintained up to 200 °C are mainly related to the fine grain size and the main strengthening phase $Al_{11}Ce_3$, which is present in a high volume fraction, and possesses fine acicular morphology and relatively good thermal stability. The improved corrosion resistance is attributed to the microstructure modification of the alloys and the corrosion product films.

1. Introduction

Over the last decade, the requirement to reduce the weight of car components as a result of legislation limiting CO_2 emission has created a renewed interest in magnesium (Mg) alloys [1]. Auto manufacturing companies have reduced vehicle weight by the use of magnesium die castings, which account for about 30% of the total reported consumption of Mg alloys [2]. The high-pressure die-cast (HPDC) Mg–Al-based alloys like AZ91D and AM60B are widely used in non-critical parts such as valve covers and instrument panels due to their excellent combination of die castability, room-temperature mechanical properties and corrosion resistance [3,4]. However, the applications of these alloys are still limited because of their poor creep resistance at temperatures above 125 °C [5,6].

In recent years, improving the elevated temperature properties has become a critical issue for the potential applications of Mg alloys in major powertrain applications [7,8]. It has been reported that the elevated temperature properties of Mg–Al alloys can be improved by the addition of elements such as RE [9–15], Ca [2,6,16], Sr [2,17], Si [4,5,18], Sn [5] and Sb [4,18]. Among them Mg–Al–RE system is a major development in heat-resistant Mg–Al-based alloys. AE42 (Mg–4Al–2RE, wt.%), a benchmark heat-resistant HPDC Mg alloy, exhibits major improvement in creep resistance, which is commonly thought to arise from the suppression of $Mg_{17}Al_{12}$ phase due to the preferential reaction of Al and RE to form the highly thermally stable $Al_{11}RE_3$ and Al_2RE intermetallic phases [19]. However, the deterioration in creep resistance of AE42 at temperature above 150 °C was also reported, and the related mechanism was still in dispute. Powell et al. [20] mainly attributed the poor creep resistance of AE42 at 175 °C to the instability and partial decomposition of $Al_{11}RE_3$ phase. While the recent work by Zhu et al. [21] showed that both Al_2RE and $Al_{11}RE_3$ phases were stable at temperature up to 200 °C, with no decomposition observed even after 2 weeks. According to their work, continuous precipitation of $Mg_{17}Al_{12}$ due to the supersaturation of Al solute in Mg matrix was responsible for the loss of creep resistance. Recently, a new HPDC alloy, AE44 (Mg–4Al–4RE, wt.%), was developed by Hydro Magnesium. The heat-resistance of AE44 alloy is further improved due to the higher RE content [21].

The typical composition of Ce-rich mischmetal added in AE42 and AE44 is 52–55 wt.% Ce, 23–25 wt.% La, 16–20 wt.% Nd, and 5–6 wt.% Pr [20,22]. The microstructures and performances of these HPDC alloys containing Ce-rich mischmetal are determined by the combined action of above all RE elements, thus it is difficult to confirm the effect of single RE element in these alloys. Wang et al. [12] reported that addition of Ce could improve the microstructure and enhance the mechanical properties of as-cast and hot-rolled Mg–5Al–0.3Mn alloy. The influences of single La, Pr and Nd on the microstructure and mechanical properties of HPDC Mg–4Al-based alloy have been studied, and the results indicate that the behav-

* Corresponding authors. Tel.: +86 451 82533026; fax: +86 451 82533026.
E-mail address: jinghuaizhang@gmail.com (J. Zhang).

0925-8388/$ – see front matter © 2010 Elsevier B.V. All rights reserved.
doi:10.1016/j.jallcom.2010.09.185

Table 1
Chemical compositions of the studied alloys (wt.%).

Alloys	Al	Ce	Mn	Fe	Mg
AM40	3.80	/	0.36	0.021	Bal.
AlCe41	4.16	1.41	0.23	0.030	Bal.
AlCe42	4.07	2.27	0.24	0.018	Bal.
AlCe44	3.82	3.93	0.27	0.020	Bal.
AlCe46	3.68	5.53	0.21	0.022	Bal.

ior of these alloys could be affected by the kind of RE elements to a certain extent [13–15]. In order to further confirm the effects of different RE elements in HPDC Mg–4Al-based alloy, in this work, the microstructure, mechanical properties and corrosion behavior of HPDC Mg–4Al–*x*Ce–0.3Mn (*x* = 0, 1, 2, 4, 6 wt.%) alloys were investigated in detail.

2. Experimental procedures

The nominal compositions (wt.%) of investigated alloys were Mg–4Al–0.3Mn, Mg–4Al–1Ce–0.3Mn, Mg–4Al–2Ce–0.3Mn, Mg–4Al–4Ce–0.3Mn and Mg–4Al–6Ce–0.3Mn, while the reference alloy was commercial AE44 containing Ce-rich mischmetal. Commercial pure Mg and Al were used, Mn and Ce were added in the form of Al–10 wt.% Mn and Mg–20 wt.% Ce master alloys, respectively. Specimens were produced using a 280 tonnes clamping force cold chamber die-cast machine. The metal was hand-ladled into the die casting machine and this required a melt temperature which was about 40 °C higher than that normally used for casting with an automated metering system involving a pump and heated tube. The melt temperature of 700 °C prior to casting was used. The die was equipped with an oil heating/cooling system and the temperature of the oil heater was set to 210 °C. The chemical compositions of the specimens were determined by inductively coupled plasma atomic emission spectroscopy (ICP-AES) and the results were listed in Table 1, in which the compositions of alloys named as AM40, AlCe41, AlCe42, AlCe44 and AlCe46 were given.

The tensile samples were 75 mm in gauge length and 6 mm in gauge diameter. Tensile tests were performed using Instron 5869 tensile testing machine at room temperature (RT) and elevated temperatures under a strain rate of $1.1 \times 10^{-3}\ s^{-1}$. The tensile creep tests were carried out on the specimens of cylindrical geometry with a 100 mm gauge length and 10 mm diameter cross-section. The value of the tensile and creep data in the study was the average of at least four measurements. The microstructures and strengthening phases of the alloys were characterized by field emission scanning electron microscope (FESEM) equipped with an energy dispersive X-ray spectrometer (EDS), transmission electron microscope (TEM) and X-ray diffraction (XRD).

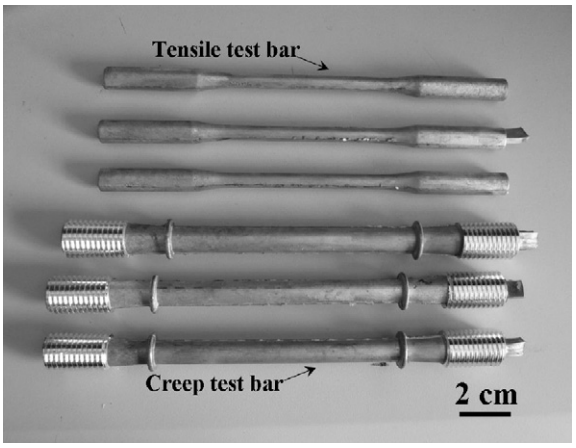

Fig. 1. Examples of the die-cast bar obtained from AlCe44 alloy.

The corrosion specimens were polished successively on finer grades of emery papers up to 800 levels. Corrosion tests were performed using standard salt spray corrosion chamber in neutral 5 wt.% NaCl. Cleaning of the specimens was done by dipping in a 400 ml aqueous solution of 10% CrO_3 + 1% $AgNO_3$ in boiling condition. The weight loss was measured by an electronic balance with an accuracy of 10^{-4} g. The extent of corrosion was given in weight loss per surface area and time (mg cm^{-2} day^{-1}, or MCD). All the reported values were averaged on at least three specimens.

3. Results and discussion

3.1. Microstructure

Fig. 1 shows the representative tensile and creep test bars obtained from the HPDC AlCe44 alloy castings. It can be observed

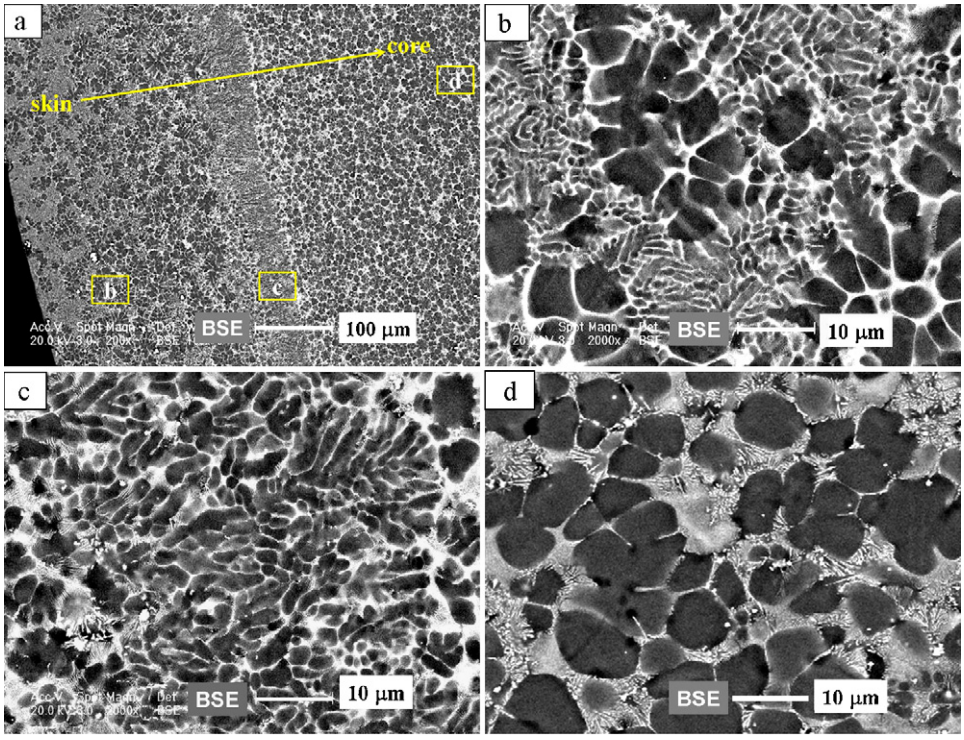

Fig. 2. Typical cross-section microstructure of the test bar obtained from HPDC AlCe44 alloy: (a) low magnification image; (b) microstructure of skin region; (c) microstructure of narrow band; (d) microstructure of interior region.

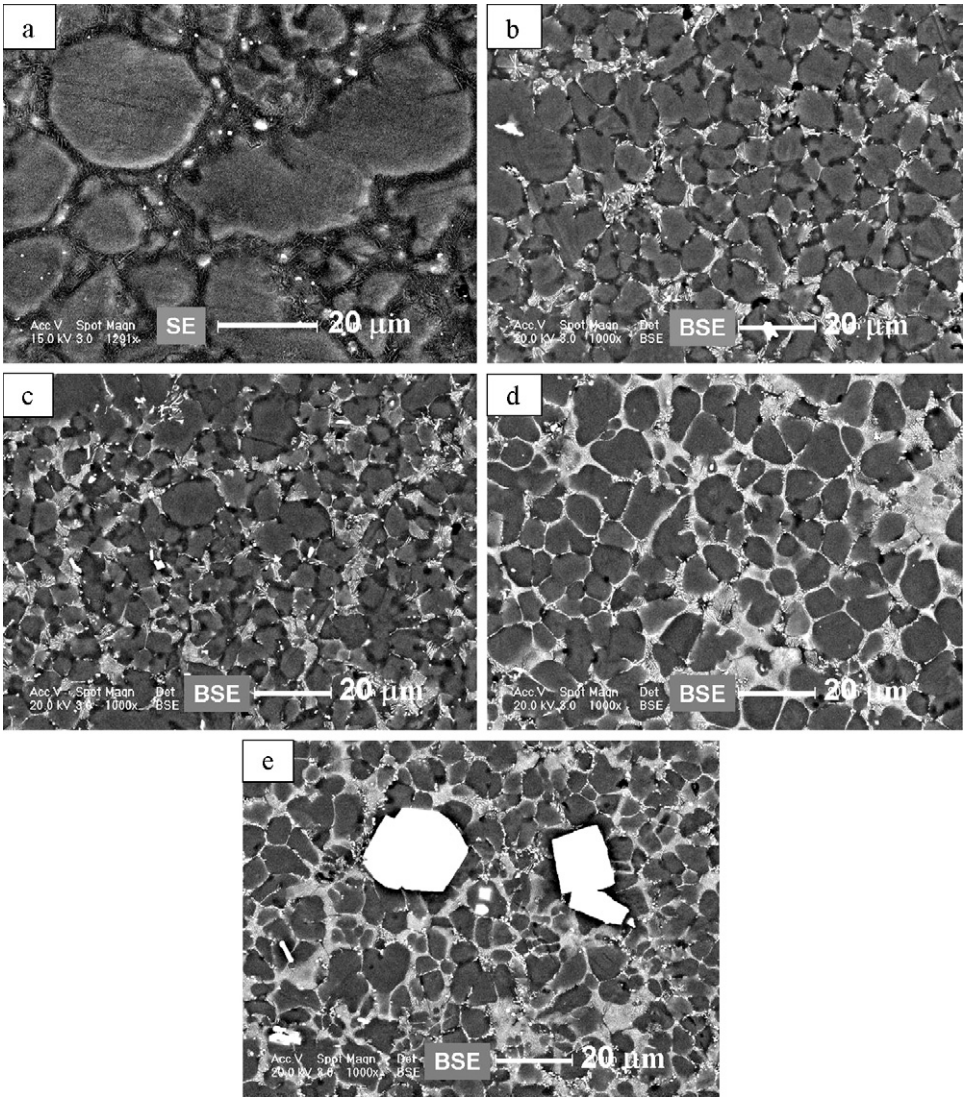

Fig. 3. Interior region microstructures of the HPDC alloys: (a) AM40; (b) AlCe41; (c) AlCe42; (d) AlCe44; (e) AlCe46.

that the die-cast samples do not present any macroscopic defect on the surface, a result that partly confirms the good die-castability of these Mg–Al–Ce–Mn alloys. The metallographic samples were cut from the middle portion of the tensile test bars.

Fig. 2(a) shows the typical cross-section microstructure of the HPDC AlCe44 alloy. A narrow band that follows a contour parallel approximately to the surface of the casting divides the alloy bar into the skin region and the interior region. It can be found that the microstructures are distinctly different in skin region (marked as b), narrow band area (marked as c) and interior region (marked as d). The thickness of skin region is about 270 μm, and, as shown in Fig. 2(b), it is composed of the fine and relatively large dendrites which are interlaced with one another, as well as the eutectics concentrated near the dendrite boundaries. The average dendritic arm spacing (DAS) of the fine dendrites is only 1 μm and that of the relatively large dendrites is about 7 μm. The thickness of narrow band is about 50 μm and it consists of fine dendrites and eutectics (Fig. 2(c)). The relatively coarse equiaxed dendrites and the eutectic structures distributed around grain boundaries constitute the interior region (Fig. 2(d)), and the DAS increases gradually up to about 9 μm with the distance close to centre of the bar. The change of the DAS from surface to centre is mainly related to the decrease of cooling rate during the solidification process. The very thin skin layer may be removed by machining, and thus its importance is not clear in industrial application.

Fig. 3 shows the comparative observations on interior region microstructures of the five HPDC Mg–4Al–*x*Ce–0.3Mn alloys. A distinctive change in the microstructure can be clearly observed with Ce addition. On the one hand, the DAS of the alloys decreases remarkably and becomes more uniform with increasing Ce content. The specific variation of the grain size with the increase of Ce content is illustrated in Fig. 4. On the other hand, with the increasing Ce content, the volume fraction of secondary phases (white constituent in FESEM images) contained in eutectics increases remarkably, and the distribution of secondary phase particles (or rather the eutectics) changes from discontinuous to continuous at this magnification. In addition, large polygonal particles with size up to 10–20 μm are observed in alloy AlCe46 containing 5.5 wt.% Ce (Table 1).

3.2. Strengthening phases

XRD patterns of the studied HPDC alloys are illustrated in Fig. 5. AM40 alloy is composed of α-Mg and β-$Mg_{17}Al_{12}$ phases. While as shown in the figure, due to addition of Ce, the diffraction peaks of β-$Mg_{17}Al_{12}$ phase decrease sharply, and finally it goes beyond

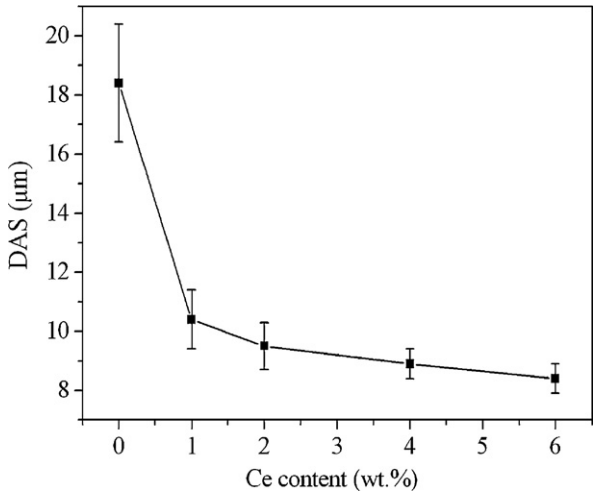

Fig. 4. Effect of Ce content on the DAS of HPDC alloys.

the detection limit of XRD. The main secondary phases in the four AlCe alloys are $Al_{11}Ce_3$ and $(Al, Mg)_2Ce$ with the former being the dominant one.

The typical magnified FESEM backscattered electron image revealing the secondary phases in the interior region in HPDC AlCe44 alloy is shown in Fig. 6(a). It is evident that there are two types of particles. The dominant secondary phase particles are the acicular ones with diameter close to 100 nm and length up to several microns, which are almost parallel and densely spaced. Besides, a small amount of polygonal particles with size about 0.3–1 μm are distributed among acicular ones. EDS analysis results of the above two phases are shown in Fig. 6(b) and (c), respectively. However, due to so fine size of particles, the Mg signal coming from matrix Mg was detected inevitably. Therefore the phase composition identified only by EDS is unreliable, although additional information may be obtained by XRD results. Fig. 7 shows the TEM images of the two types of particles. The diffraction patterns corresponding to the acicular phase and polygonal phase further confirm that the former is $Al_{11}Ce_3$ (body-centered orthorhombic structure, $a = 0.4395$ nm, $b = 1.3025$ nm, $c = 1.0092$ nm [23]) and the latter is $(Al, Mg)_2Ce$ (Al_2Ce, face-centered cubic structure, $a = 0.7700$ nm [23]).

Here, it should be noted that according to the extensive work on the ternary Mg–Al–Ce phase diagram by Gröbner et al. [24] the binary Al_2Ce phase dissolves significant amounts of Mg, and the correct designation of Al_2Ce should be $(Al, Mg)_2Ce$ solid solution phase with a ternary composition, though the detection of $(Al, Mg)_2Ce$ using XRD, EDS and diffraction pattern is complicated by the fact that this phase is a solid solution, while no solubility is assumed for $Al_{11}Ce_3$ phase.

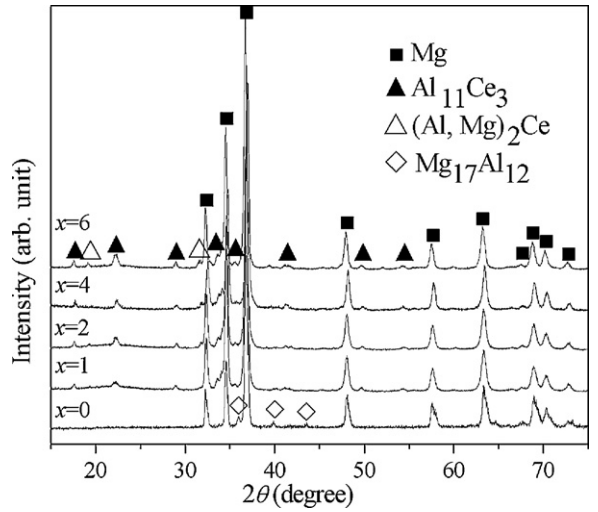

Fig. 5. XRD patterns of the HPDC Mg–4Al–*x*Ce–0.3Mn alloys.

Table 2
Ultimate tensile strength (UTS) of the HPDC alloys.

Alloys	UTS (MPa)						
	RT	120 °C	150 °C	175 °C	200 °C	250 °C	300 °C
AM40	218	128	119	97	80	66	57
AlCe41	232	173	144	138	111	91	70
AlCe42	247	178	148	142	114	95	73
AlCe44	250	184	154	145	123	107	80
AlCe46	254	187	157	138	118	104	82
AE44	247	176	157	136	120		

Table 3
Tensile yield strength (TYS) of the HPDC alloys.

Alloys	TYS (MPa)						
	RT	120 °C	150 °C	175 °C	200 °C	250 °C	300 °C
AM40	120	85	79	72	60	55	51
AlCe41	146	117	107	105	98	81	67
AlCe42	148	120	109	106	100	84	69
AlCe44	157	129	123	114	106	93	77
AlCe46	161	134	127	120	106	94	78
AE44	147	124	123	107	100		

Fig. 8(a) presents the element area profiles in HPDC AlCe44 alloy. It can be seen that Al and Ce elements mostly form Al–Ce compounds in the grain boundary areas. Mn is almost homogeneously distributed in the matrix, even though few areas contain very high concentration of this element. It can be deduced that a few polygonal Al–Ce–Mn compound particles formed in the matrix. This is a new phase which is not detected in Fig. 6, and its (point A) EDS microanalysis is shown in Fig. 8(b). The result shows that the proportion of Al, Ce and Mn is Al52.24Ce9.64Mn28.01, and, as a result, the particle can be described as $Al_{10}Ce_2Mn_7$. The similar phase $Al_{10}RE_2Mn_7$ was also found in the HPDC AE42 alloy, whose diffraction patterns were indexed according to a hexagonal system [25]. However, the content of this Mn-containing phase is so low in the Mg–Al–Ce-based alloys that it cannot be detected by XRD. In view of its trace, it is believed that this Mn-containing compound has little effect on the performance of alloy.

3.3. Mechanical properties

Fig. 9 shows the typical tensile stress–strain curves of HPDC Mg–4Al–*x*Ce–0.3Mn alloys at different testing temperatures. The tensile properties including ultimate tensile strength (UTS), tensile yield strength (TYS) and elongation to failure (ε) from room temperature (RT) to 300 °C are listed in Tables 2–4, respectively. The analysis of these data reveals that the Mg–4Al–0.3Mn alloy has the lowest tensile strength; the tensile strength increases with adding

Table 4
Elongation to failure (ε) of the HPDC alloys.

Alloys	ε (%)						
	RT	120 °C	150 °C	175 °C	200 °C	250 °C	300 °C
AM40	9	15	17	18	17	12	11
AlCe41	9	18	21	25	18	15	16
AlCe42	12	19	24	25	23	21	20
AlCe44	11	26	25	25	21	20	16
AlCe46	10	29	22	22	21	20	17
AE44	11	22	25	26	24		

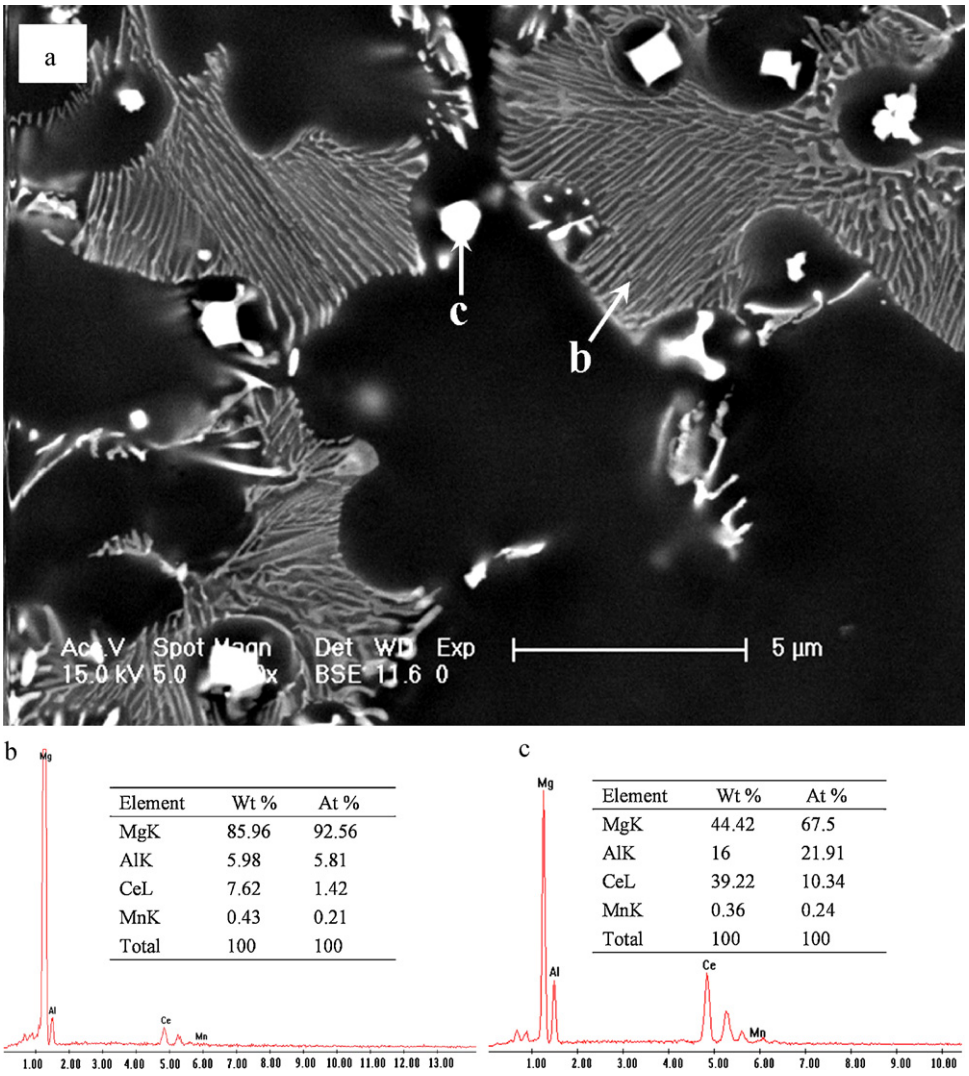

Element	Wt %	At %
MgK	85.96	92.56
AlK	5.98	5.81
CeL	7.62	1.42
MnK	0.43	0.21
Total	100	100

Element	Wt %	At %
MgK	44.42	67.5
AlK	16	21.91
CeL	39.22	10.34
MnK	0.36	0.24
Total	100	100

Fig. 6. (a) Backscattered FESEM micrograph of the secondary phases with (b) and (c) EDS results of point b and c in (a) in HPDC AlCe44 alloy.

Ce from 1 wt.% to 4 wt.%, especially at high temperatures, but it changes only slightly when the content of this element rises above 4 wt.%. The high temperature strength is reasonably constant (i.e., both UTS and TYS stay above 100 MPa at 200 °C), for Ce contents of about 4 wt.%. A further increase in temperature to 300 °C causes the properties of all the alloys to sharply deteriorate.

The tensile creep tests of HPDC AlCe44 alloy were carried out to further study its high temperature mechanical properties. Fig. 10

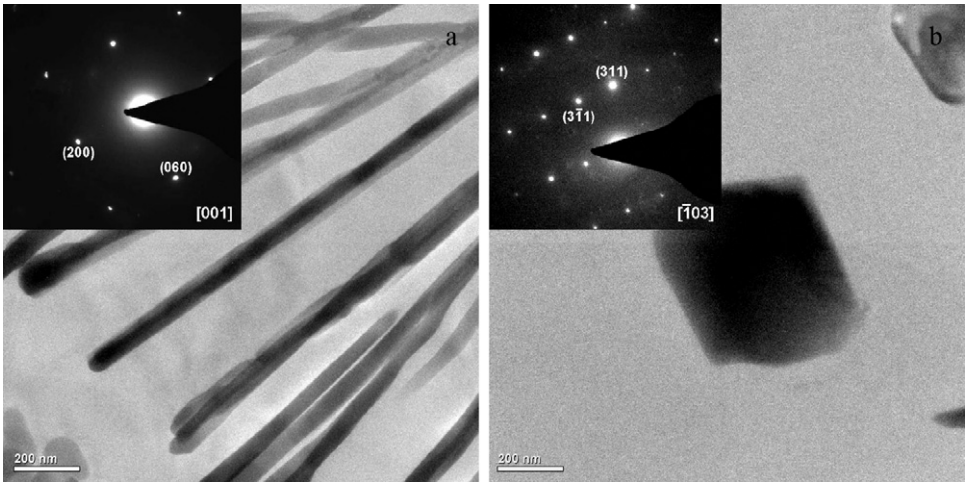

Fig. 7. TEM images with diffraction patterns of (a) acicular particle and (b) polygonal particle.

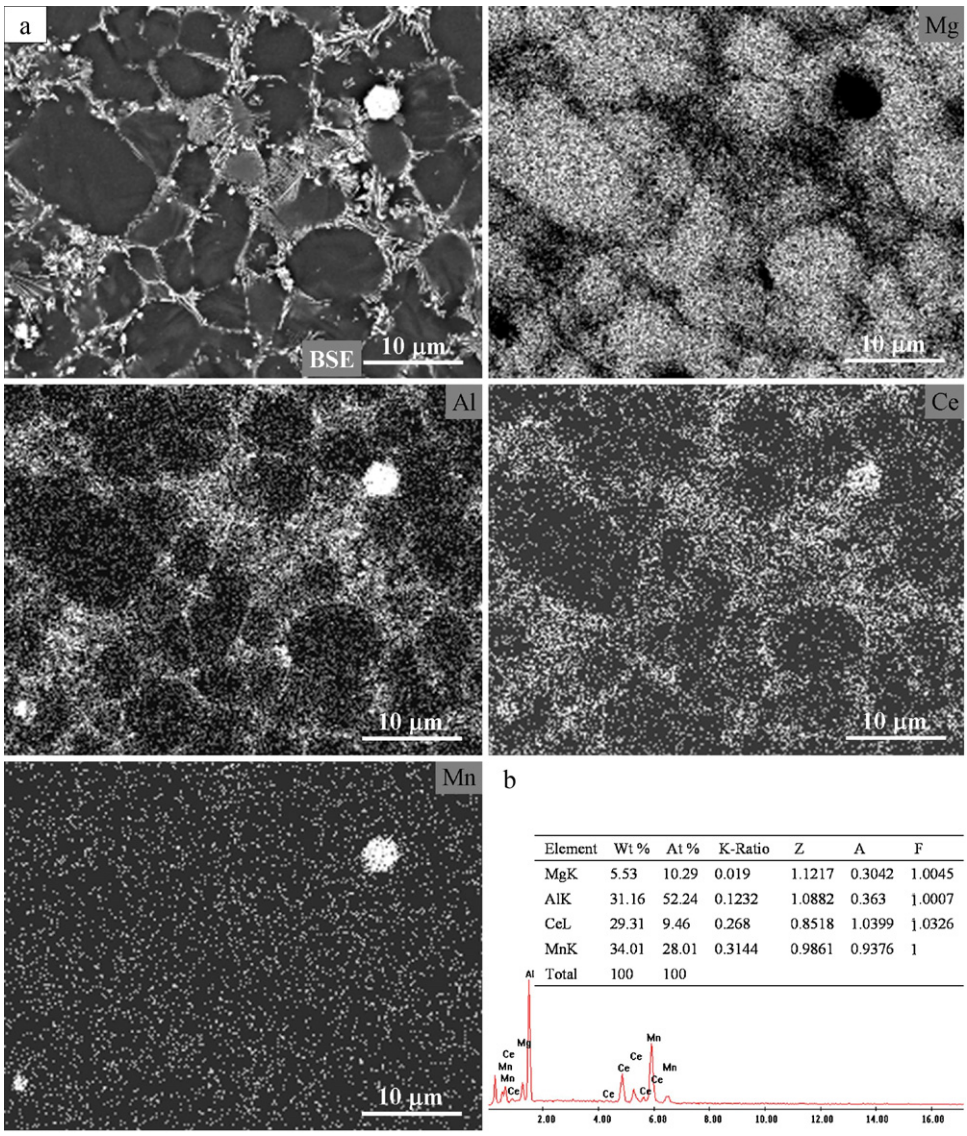

Fig. 8. (a) Map distributions of Mg, Al, Ce, Mn in HPDC AlCe44 alloy and (b) EDS results of the point A in (a).

shows the typical tensile creep curve of HPDC AlCe44 alloy compared with that of the two reference HPDC alloys, namely, AZ91 and AE44. Among them AZ91 is the most popular HPDC magnesium alloy used currently and AE44 is the typical heat-resistant alloy developed in recent years, which has been successfully used for producing powertrain components [26]. The creep tests were carried out at 200 °C under a load of 70 MPa for AlCe44 and AE44 alloys, while 150 °C/70 MPa for AZ91 alloy considering its poor high-temperature properties. As shown in the figure, AlCe44 alloy exhibits a lower creep resistance compared with that of AE44 alloy in the same test condition. There is no way to positively say that a true steady state has been reached at 100 h, in view of this, only the strain rate at 96 h is given, and it is about 2.79×10^{-8} s^{-1} for AlCe44 alloy, while it is about 6.94×10^{-9} s^{-1} for AE44 alloy. As expected, the creep behavior of the AlCe44 is by far better than that of the AZ91 alloy.

In the previous studies [13–15], the effect of La, Pr and Nd on the microstructure and mechanical properties of HPDC AM40 alloy has been investigated. The UTS, TYS and ε of Mg–4Al–xRE–0.3Mn (x = 0, 1 and 6 wt.%, RE = La, Ce, Pr and Nd) alloys at RT and 200 °C are listed in Table 5. It indicates that all the four RE elements can improve the mechanical properties of Mg–4Al-based alloy, and strengthening effect increases with increasing RE content. The difference of strengthening effect is small when RE content is low, while the AlLa alloys containing La (e.g., AlLa46) exhibit the best mechanical properties when RE content increases. In addition, the researches by now indicate that compared with Ce, La is more effective for the improvement of creep resistance, however, the price of Ce is lower than that of La and much lower than that of Pr and Nd.

Table 5
Mechanical properties of the HPDC Mg–4Al–xRE–0.3Mn (x = 0, 1 and 6 wt.%, RE = La, Ce, Pr and Nd).

Alloys	RT			200 °C		
	UTS (MPa)	TYS (MPa)	ε (%)	UTS (MPa)	TYS (MPa)	ε (%)
AM40	218	120	9	80	60	17
AlLa41	236	133	12	117	89	20
AlCe41	232	146	9	111	98	18
AlPr41	241	145	13	114	96	27
AlNd41	244	148	12	101	86	33
AlLa46	257	171	7	136	115	18
AlCe46	254	161	10	118	106	21
AlPr46	251	155	10	117	110	33
AlNd46	261	165	12	115	102	32

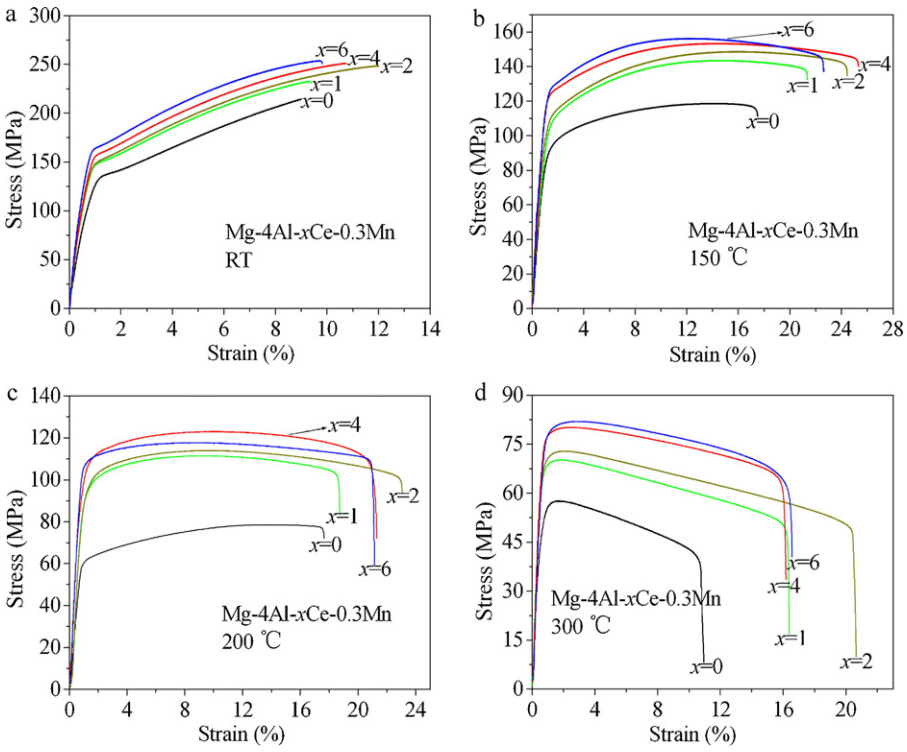

Fig. 9. Typical tensile stress–strain curves of the HPDC alloys at different temperatures.

3.4. Strengthening mechanism

Addition of Ce especially up to 4 wt.% can remarkably improve the mechanical properties of Mg–4Al-based alloy when the test temperature does not exceed 200 °C. This behavior could be related to the considerable strengthening role played by the fine DAS of the Ce-containing alloys, a consequence of the extremely high cooling rate and the constitutional supercooling effect of Ce and Al. The reduction of DAS due to the supercooling refining effect of Ce can be explained as follows: during the solidification process, Ce atoms aggregate at the solid/liquid interface, and this effect results in constitutional supercooling in the diffusion layer ahead of the advancing solid/liquid interface and the reduction of atomic diffusion rate. Thus, the primary α-Mg grain growth is restricted [27,28]. Furthermore, constitutional supercooling is a major force for nucleation [29]. In addition, with the continuous decrease in the melt temperature the enrichment of solute atoms leads to the formation of intermetallic compounds which mainly distribute in the grain boundary areas, thus the α-Mg grain growth is further restricted.

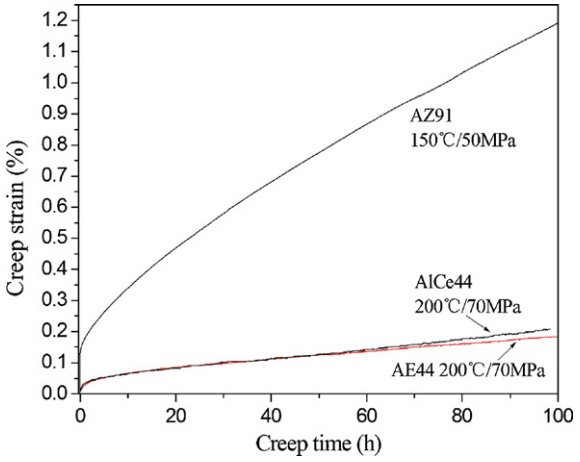

Fig. 10. Typical tensile creep curves of the HPDC AlCe44, AE44 and AZ91 alloys.

On the other hand, in AM40 alloy as well as in AZ91 alloy, the main strengthening phase is $Mg_{17}Al_{12}$, which has a low melting point (with a eutectic temperature of 437 °C) and a poor thermal stability. $Mg_{17}Al_{12}$ phase can readily soften and coarsen at the temperature exceeding 125 °C [30]. Addition of Ce to AM40 results in the suppression of $Mg_{17}Al_{12}$ phase and the formation of $Al_{11}Ce_3$ and Al_2Ce phases. Al–Ce phases have much high melting points (>1200 °C), and then the softening temperature of the alloy containing Al–Ce phases can be increased. As a result during straining the fine Al–Ce particles which occupy a large grain boundary area can block the grain boundary sliding very effectively, especially at elevated temperatures. With the increase of Ce content in the alloys, the amount of Al–Ce particles increases significantly, and then the strengthening effect is also improved. Of course, it should be noted that besides the volume fraction other characteristics such as size, morphology as well as distribution of the secondary phase particles could influence the mechanical properties of alloys to some extent. Generally the grain refinement is also an effective means to improve ductility. However, the HPDC AlCe46 alloy with the lowest DAS does not obtain the optimal ductility among the studied alloys. We consider that the Al_2Ce particles with coarse size in AlCe46 alloy should be responsible for this phenomenon. Fig. 11 shows FESEM images of the tensile fracture surface of AlCe46 alloy tested at RT. The fracture observation mainly indicates that the large Al_2Ce particles are located in the bottom of the pits surrounded with tearing ridges, and they would be cracked during the tensile tests to relieve the mismatch of plastic deformation between secondary phase and Mg matrix. In addition, the crystal structure of Al_2Ce is face-centered cube (fcc, $a = 0.770$ nm) incoherent with that of Mg matrix (hexagonal close packed, hcp, $a = 0.3202$ nm, $c = 0.5199$ nm), which readily leads to the fragility of Mg/Al_2Ce interface [30]. This analysis suggests that the big brittle Al_2Ce phase particles could cause harmful influences on the tensile properties of AlCe46 alloy. On the other hand, the reinforcing effect of secondary phase is inadequate

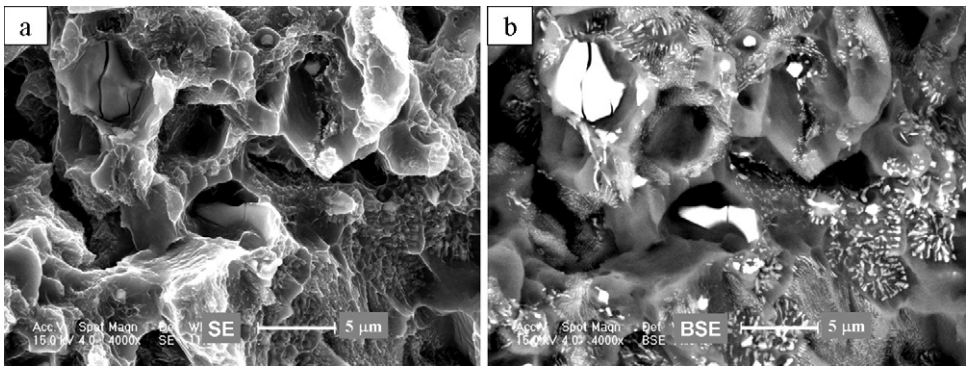

Fig. 11. FESEM observation of the fracture surface of HPDC AlCe46 alloy: (a) secondary electron image, and (b) backscattered electron image.

when Ce content is less than 4 wt.% (i.e., 1 wt.% or 2 wt.%) in the Mg–4Al-based alloy. An obvious conclusion is that the HPDC AlCe44 containing about 4 wt.% Ce has the more reasonable cost performance ratio as a high-performance heat-resistant alloy, although the temperature limit for industrial applications does not exceed 200 °C.

3.5. Corrosion behavior

Fig. 12 illustrates the curve of corrosion rates of the HPDC Mg–4Al–*x*Ce–0.3Mn alloys under salt spraying at 35 °C for 4 days. It can be observed that the corrosion rate decreases remarkably with adding Ce until 4 wt.%, while a further increase in Ce determines a deterioration of the corrosion resistance. The corrosion rate of AlCe44 alloy which has the best corrosion resistance is about 1–2 times higher than that of AZ91 alloy (~0.1 MCD) [31]. Considering the relatively high impurity Fe content in the studied alloys (Table 1), it is believed that the corrosion resistance of these materials can be further improved through reducing Fe content.

Fig. 13 shows the typical corrosion morphologies of AM40 and AlCe44 after 4 days salt-spray tests. In the case of AM40 alloy as shown in Fig. 12(a) and (b), most surfaces suffer serious corrosion, and the morphology of the corroded surface consists of a series of deep corrosion pits with size of 20–50 μm. Analysis suggests that for AM40 alloy corrosion originates in the interior of the α-Mg grains, although the corrosion resistance of grain boundary is higher than that of matrix, it is still not enough to impede the corrosion propagation from one grain to another. However, for AlCe44 alloy the severe corrosion only occurs in the fine α-Mg grains and the corrosion pits are relatively shallow. The α-Mg refined grains are surrounded by $Al_{11}Ce_3$ acicular particles, as an effect of Ce addition to AM40 alloy; as a result, when the alloys contain a high Ce content, the finely spaced $Al_{11}Ce_3$ acicular particles almost separate the α-Mg grains. The corrosion of α-Mg grains, which act as anode, is thus delayed. On the other hand, though the Al–Ce phases act as a micro-galvanic cathode relative to the Mg matrix, the potential difference between them is relatively small, and the Al–RE phases can be passivated in a wide range of pH [32,33]. Therefore, the formation of Al–Ce phases brings a more positive effect as corrosion barriers than a negative one as galvanic cathode accelerating corrosion. As for the increasing trend of corrosion rate when Ce content is above 4 wt.%, it is considered to be associated with the large Al_2Ce particles which appear only in the alloy AlCe46 containing 5.5 wt.% Ce (Table 1).

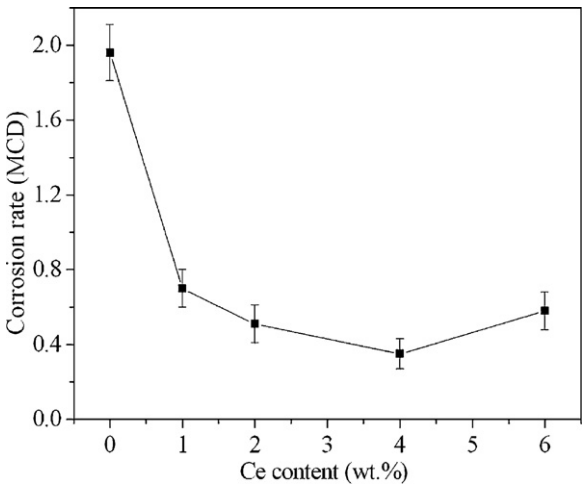

Fig. 12. Weight loss corrosion rates of the HPDC alloys.

Fig. 14(a) and (b) shows the typical FESEM micrographs of the corrosion products formed on the surfaces of AM40 and AlCe44 alloys, respectively. Though both corrosion products are composed of voluminous tiny flakes, the size of the flakes decreases and the compactness of corrosion film increases with the addition of Ce.

EDS analyses of both corrosion products are revealed in Fig. 14(c) and (d), respectively. The participation of RE elements in the corrosion film is thought to be beneficial to the corrosion resistance of the alloys. Rosalbino et al. [34] attributed the improved corrosion behavior of the Mg–Al–Er alloys to the incorporation of erbium in $Mg(OH)_2$ lattice in the corrosion film. The incorporation of Y_2O_3 in the passive film was given by Yao et al. [35] as the reason for the enhanced passivity properties of melt-spun Mg–Y alloys. Liu et al. [9] believed that RE elements promoted the formation of Al–RE oxide and hydroxide, and made the corrosion product of AM60-RE alloys more compact. Chang et al. [36] suggested that the corrosion products of Mg–*x*Gd–3Y–0.4Zr alloys were stabilized by Gd and Y from the results of AES. In this work, the major observation of EDS results as shown in Fig. 13(c) and (d) is the enrichment of Ce and Al in the corrosion film of AlCe44 alloy. The protective characteristic is related with the so-called Pilling–Bedworth ratio (PBR, the ratio of oxide volume to the volume of original element which was consumed to form the oxide) criterion to some extent. The PBR of magnesium oxide, cerium oxide and aluminum oxide are 0.78, 1.16 and 1.28, respectively [37]. Therefore, the film containing cerium oxide and aluminum oxide with PBR > 1 could become more compact and protective. Furthermore, the incorporation of Ce and Al in the brucite layered structure of the corrosion product film can increase the local positive charge, which could be balanced by trapping Cl^- and CO_3^{2-}, and it is beneficial to obstruct the penetration of the detrimental anions in the brucite layers, thus further corrosion is inhibited [38].

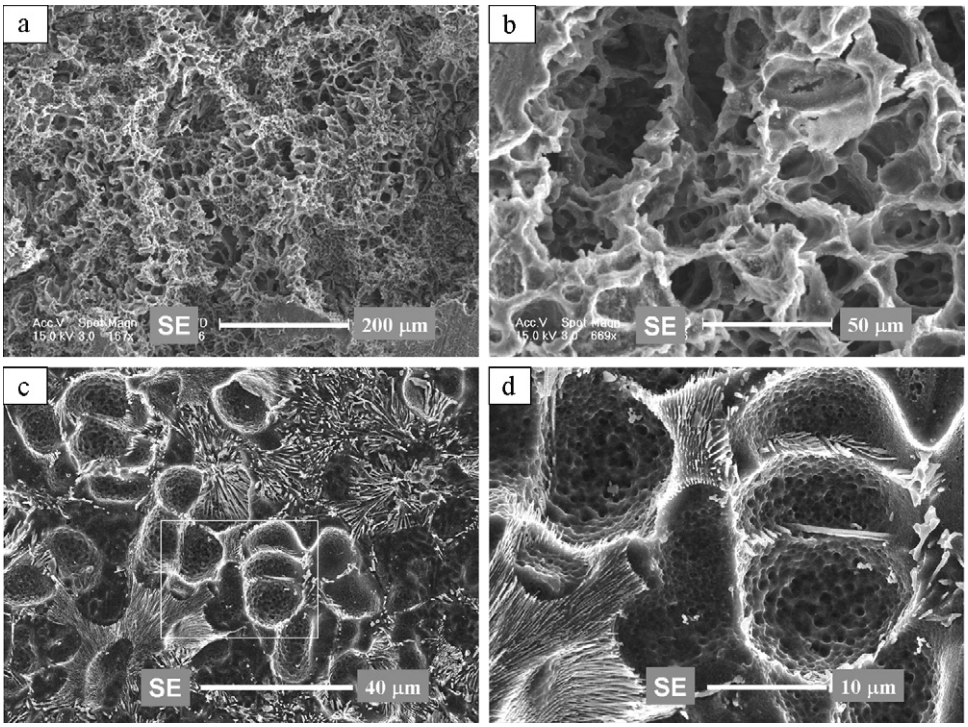

Fig. 13. Typical FESEM images of corrosion surface morphology: (a) low and (b) high magnification images of HPDC AM40 alloy; (c) low and (d) high magnification images of HPDC AlCe44 alloy.

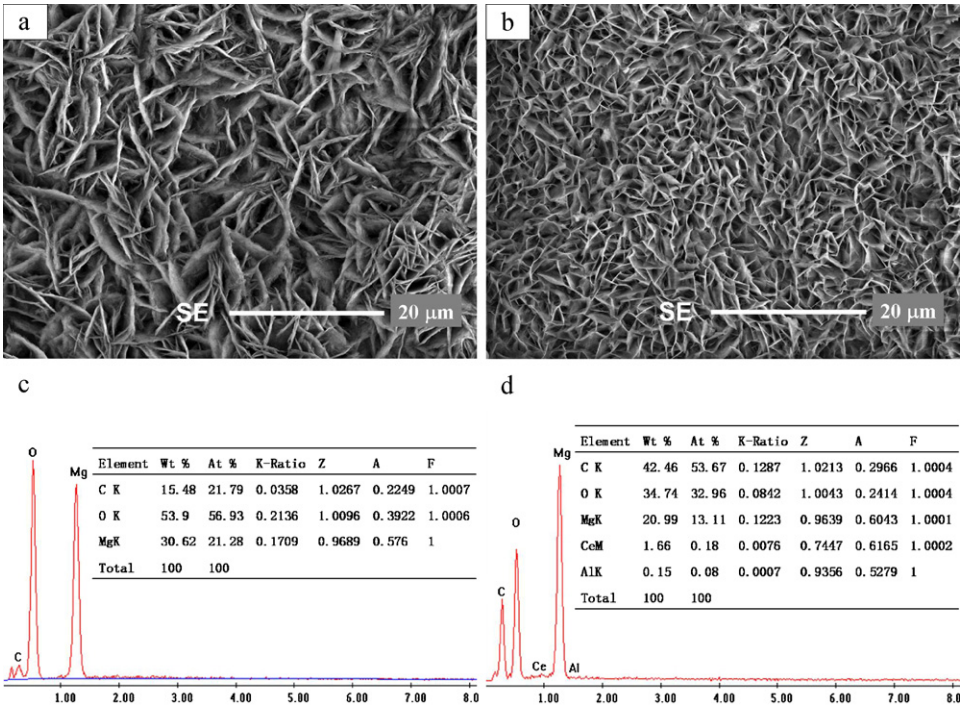

Element	Wt %	At %	K-Ratio	Z	A	F
C K	15.48	21.79	0.0358	1.0267	0.2249	1.0007
O K	53.9	56.93	0.2136	1.0096	0.3922	1.0006
MgK	30.62	21.28	0.1709	0.9689	0.576	1
Total	100	100				

Element	Wt %	At %	K-Ratio	Z	A	F
C K	42.46	53.67	0.1287	1.0213	0.2966	1.0004
O K	34.74	32.96	0.0842	1.0043	0.2414	1.0004
MgK	20.99	13.11	0.1223	0.9639	0.6043	1.0001
CeM	1.66	0.18	0.0076	0.7447	0.6165	1.0002
AlK	0.15	0.08	0.0007	0.9356	0.5279	1
Total	100	100				

Fig. 14. FESEM images of corrosion product film formed on the surfaces of (a) AM40 and (b) AlCe44 alloys, EDS results of corrosion product of (c) AM40 and (d) AlCe44 alloys.

As a consequence, the improvement of corrosion resistance of HPDC AM40 alloy with Ce addition is related to two key factors. Addition of Ce can not only change the microstructure of the Mg–4Al-based alloy to improve the corrosion resistance, but also change the composition and compactness of corrosion product film to enhance the protective effectiveness.

4. Conclusions

The microstructure, strengthening phases, mechanical properties and corrosion behavior of high-pressure die-cast Mg–4Al–*x*Ce–0.3Mn (x = 0, 1, 2, 4 and 6 wt.%) alloys have been investigated. The main conclusions can be drawn as follows:

(1) The Mg–4Al–*x*Ce–0.3Mn alloys exhibit an excellent die-castability. A narrow band with a fine structure divides the cross-section of test bar into the fine skin region and the relatively coarse interior region.
(2) With addition of Ce, the grains of Mg–4Al–0.3Mn alloy are refined and the secondary phase $Mg_{17}Al_{12}$ is suppressed and substituted by $Al_{11}Ce_3$ and $(Al, Mg)_2Ce$ with the former being the dominant one.
(3) Mg–4Al–4Ce–0.3Mn alloy has the best cost performance ratio. The excellent mechanical properties are retained up to 200 °C, and they are the results of the fine dendritic arm spacing and the strengthening effect played by a high volume fraction of precipitates. The $Al_{11}Ce_3$ particles are located in grain boundary areas, and possess fine acicular morphology and relatively good thermal stability. The improved corrosion resistance is related to the microstructure change of the alloys and the corrosion product films.

Acknowledgements

This work was supported by the National Natural Science Foundation of China (no. 50871033), the Key Project of Science and Technology of Harbin City (2008AA4CH044, 2009AA1AG065, 2010AA4BE031), the Fundamental Research funds for the Central Universities (HEUCF101001), the Heilongjiang Postdoctorial Fund (LBH-Z09217) and China Postdoctoral Science Foundation (20100471015).

References

[1] M.K. Kulekei, Int. J. Adv. Manuf. Technol. 39 (2008) 851–865.
[2] L. Shang, I.H. Jung, S. Yue, R. Verma, E. Essadiqi, J. Alloys Compd. 492 (2010) 173–183.
[3] H. Gjestland, H. Westengen, Adv. Eng. Mater. 9 (2007) 769–776.
[4] A. Srinivasan, J. Swaminathan, M.K. Gunjan, U.T.S. Pillai, B.C. Pai, Mater. Sci. Eng. A 527 (2010) 1395–1403.
[5] B.H. Kim, S.W. Lee, Y.H. Park, I.M. Park, J. Alloys Compd. 493 (2010) 502–506.
[6] B. Kondori, R. Mahmudi, Mater. Sci. Eng. A 527 (2010) 2014–2021.
[7] A.A. Luo, Int. Mater. Rev. 49 (2004) 13–30.
[8] M.O. Pekguleryuz, A.A. Kaya, Adv. Eng. Mater. 5 (2003) 866–878.
[9] W. Liu, F. Cao, L. Chang, Z. Zhang, J. Zhang, Corros. Sci. 51 (2009) 1334–1343.
[10] J. Wang, H. Dong, L. Wang, Y. Wu, L. Wang, J. Alloys Compd. 507 (2010) 178–183.
[11] B.H. Kim, K.C. Park, Y.H. Park, I.M. Park, Mater. Sci. Eng. A 527 (2010) 6372–6377.
[12] J. Wang, R. Liao, L. Wang, Y. Wu, Z. Cao, L. Wang, J. Alloys Compd. 477 (2009) 341–345.
[13] J.H. Zhang, M.L. Zhang, J. Meng, R.Z. Wu, D.X. Tang, Mater. Sci. Eng. A 527 (2010) 2527–2537.
[14] J.H. Zhang, K. Liu, D.Q. Fang, X. Qiu, P. Yu, D.X. Tang, J. Meng, J. Alloys Compd. 480 (2009) 810–819.
[15] J.H. Zhang, J. Wang, X. Qiu, D.P. Zhang, Z. Tian, X.D. Niu, D.X. Tang, J. Meng, J. Alloys Compd. 464 (2008) 556–564.
[16] J.R. TerBush, A. Suzuki, N.D. Saddock, J.W. Jones, T.M. Pollock, Scripta Mater. 58 (2008) 914–917.
[17] F. Czerwinski, A. Zielinska-Lipiec, Acta Mater. 53 (2005) 3433–3444.
[18] A. Srinivasan, J. Swaminathan, U.T.S. Pillai, Guguloth Krishna, B.C. Pai, Mater. Sci. Eng. A 485 (2008), 96-91.
[19] M.S. Dargusch, S.M. Zhu, J.F. Nie, G.L. Dunlop, Scripta Mater. 60 (2009) 116–119.
[20] B.R. Powell, V. Rezhets, M.P. Balogh, R.A. Waldo, JOM-J. Min. Met. Mat. Soc. 54 (2002) 34–38.
[21] S.M. Zhu, M.A. Gibson, J.F. Nie, M.A. Easton, T.B. Abbott, Scripta Mater. 58 (2008) 477–480.
[22] J.H. Zhang, P. Yu, K. Liu, D.Q. Fang, D.X. Tang, J. Meng, Mater. Design 30 (2009) 2372–2378.
[23] P. Villars, Pearson's Handbook of Crystallographic Data for Intermetallic Phase (Desk Edition), American Society for Metals, Metal Park, OH, 1997, Al: 37.
[24] J. Gröbner, D. Kevorkov, R. Schmid-Fetzer, Intermetallics 10 (2002) 415–422.
[25] G. Pettersen, H. Westengen, R. Hoier, O. Lohne, Mater. Sci. Eng. A 207 (1996) 115–120.
[26] P. Bakke, H. Westengen, TMS Magnesium Technol. 12 (2005) 291–296.
[27] S.S. Li, B. Tang, D.B. Zeng, J. Alloys Compd. 437 (2007) 317–321.
[28] J. Wang, J. Yang, Y. Wu, H. Zhang, L. Wang, Mater. Sci. Eng. A 472 (2008) 332–337.
[29] Y.C. Lee, A.K. Dahle, D.H. Stiohn, Metall. Mater. Trans. A 31 (2000) 2895–2906.
[30] Y. Lü, Q. Wang, X. Zeng, W. Ding, C. Zhai, Y. Zhu, Mater. Sci. Eng. A 278 (2000) 66–76.
[31] A. Luo, M.O. Pekguleryuz, J. Mater. Sci. 29 (1994) 5259–5271.
[32] G.L. Song, Corrosion and Protection of Magnesium Alloy, Chemical Industry Press, 2006, pp. 169–170.
[33] O. Lunder, K. Nisancioglu (Eds.), Progress in the Understanding and Prevention of Corrosion, 1993, pp. 1249–1254, London.
[34] F. Rosalbino, E. Angelini, S. De Negri, A. Saccone, S. Delfino, Intermetallics 13 (2005) 55–60.
[35] H.B. Yao, Y. Li, A.T.S. Wee, Electrochim. Acta 48 (2003) 4197–4204.
[36] J. Chang, X. Guo, S. He, P. Fu, L. Peng, W. Ding, Corros. Sci. 50 (2008) 166–177.
[37] W.J. Ding, Science and Technology of Magnesium Alloy, Science Press, 2006, pp. 159–160.
[38] H.B. Yao, Y. Li, A.T.S. Wee, J.S. Pan, J.W. Chai, Appl. Surf. Sci. 173 (2001) 54–61.